Direct Z-Scheme In_2S_3@$BiYWO_6$ Heterojunction Photocatalysts for Highly Efficient Environmental Remediation

Junlong Zhang, [1] Jie Wei, [1,*] Minchuan Xiahou, [1] Zehao Sun, [1] Ao Cao, [1] Youxin Yuanfeng, [1] Yanchun He, [2,] Shigeng Song [3]

[1] Electronic Materials Research Laboratory, Key Laboratory of Ministry of Education & Shaanxi Engineering Research Center of Advanced Energy Materials and Devices, School of Electronic Science and Engineering, Xi'an Jiaotong University, Xi'an 710049, P. R. China

[2] Lanzhou Institute of Physics, Lanzhou 730000, P. R. China

[3] Institute of Thin Films, Sensors and Imaging, University of the West of Scotland, SUPA Paisley PA1 2BE, Scotland, UK

***Corresponding Author**:

Jie Wei, E-mail address: weij2008@xjtu.edu.cn ; jiewei2013wj@gmail.com

Other authors:

Junlong Zhang, E-mail address: 2450773043@qq.com

Minchuan Xiahou, E-mail address: 1477795397@qq.com

Zehao Sun, E-mail address: 834787943@qq.com

Ao Cao, E-mail address: aoa7115@163.com

Youxin Yuanfeng, E-mail address: 595393477@qq.com

Yanchun He, E-mail address: heyanch@163.com

Shigeng Song, E-mail address: shigeng.song@uws.ac.uk

Abstract

Novel In_2S_3@$BiYWO_6$ heterojunction photocatalysts were designed and synthesized by a simple two-step hydrothermal method, which exhibit extremely excellent photocatalytic activity for degrading the residual antibiotics in wastewater. Especially, In_2S_3@$BiYWO_6$ composite with mass ratio of 10:1 shows the highest photo-degradation efficiency towards Tetracycline Hydrochloride, which is about 2.46 and 7.55 times than that of pristine In_2S_3 and $BiYWO_6$, respectively. A direct Z-scheme charge transfer mechanism was demonstrated in these heterojunctions through the XPS analysis, radical species trapping experiments and fluorescence detection. Within the framework of this mechanism, the critical built-in electric field (E_i) formed at the contact interface between In_2S_3 and $BiYWO_6$ spatially separates reduction or oxidation sites and thus preserves the photogenerated carriers with stronger redox ability on reaction sites, which ultimately enhances the photocatalytic activity of the heterojunction catalysts. It is commendable that such Z-scheme heterostructures between In_2S_3 and $BiYWO_6$ exist in a wide span of component ratios (from 5:1 to 30:1), which is beneficial for the environmental remediation applications. It is believed that this work provides new ideas for design and synthesis of novel Z-scheme heterojunction photocatalysts.

Keywords: In_2S_3; $BiYWO_6$; Z-scheme Heterojunction; Photocatalyst; Tetracycline Hydrochloride

1. Introduction

Recently, with the development of modern medicine, antibiotics have been widely used to inhibit or kill bacteria. However, the residual antibiotics in the waterbody have caused great impacts on the ecological balance and human health. Therefore, the removal of antibiotics from the waterbody has become a research hotspot in the field of environmental remediation [1]. Among them, Tetracycline Hydrochloride (TC-HCl) as a heavily used antibiotic is widely employed in the treatment of infectious diseases in both humans and animals. However, the residual tetracycline hydrochloride in the waterbody will eventually be ingested by human beings through the food chain. Therefore, a green and efficient degradation scheme for Tetracycline Hydrochloride is urgently needed [2]. Semiconductor-based photocatalytic technology has attracted much attention due to its green, safe, reliable, and cost-controllable advantages, and it has many applications in the field of pollutant degradation in the waterbody [3–5]. In order to utilize the photocatalysts efficiently, the photocatalysts must possess an efficient charge separation capability and a wide absorption spectral range. However, it is obvious that single-component catalysts cannot satisfy these two requirements simultaneously. The wider the absorption spectral range of a semiconductor, the narrower its band gap. Meanwhile, the photogenerated electrons from the conduction band (CB) and the holes from the valence band (VB) of such catalyst are more likely to result in a direct recombination, which would rather reduce its redox capacity [6–8]. Therefore, the construction of heterojunction photocatalysts has been proposed to make up for the insufficiency of single-component photocatalysts. In recent years, both the traditional Type-II and direct Z-scheme heterojunctions have become popular schemes for heterojunction catalysts. As shown in Fig. S1(a), within the conventional Type-II heterojunction photocatalyst, the photogenerated holes on the VB of photocatalyst I (PC-I) transfer to the VB of photocatalyst II (PC-II), while the electrons on the CB of PC-II transfer to the CB of PC-I. The direct recombination of photogenerated carriers in each catalyst is suppressed through this pathway, simultaneously leading to the bandgap reduction. However, the redox ability of the

81 photogenerated holes on the VB of PC-I and the electrons on the CB of PC-II at the reaction sites is
82 eventually weakened, which in turn reduces the catalytic ability of the Type-II heterojunction
83 photocatalyst [9–11]. Within the framework of direct Z-scheme photocatalyst, the photogenerated
84 electrons on the CB of PC-I are easily recombined with the holes on the VB of PC-II via charge
85 transfer, which inhibits the direct recombination and simultaneously retains the photogenerated
86 carriers with stronger redox capacity (e^- in PC-II or h^+ in PC-I) in each photocatalyst. It is clear that
87 the direct Z-scheme photocatalysts have better catalytic activity compared to the Type-II
88 photocatalysts [12–16].

89 Based on the above analysis, novel direct Z-scheme heterojunction photocatalysts were
90 designed and developed using reduced photocatalyst In_2S_3 and oxidised photocatalyst $BiYWO_6$ in
91 this paper. To the best of our knowledge, there is no any report on the synthesis of $In_2S_3@BiYWO_6$
92 photocatalysts with direct Z-scheme heterojunction. Recently, In_2S_3 has been widely used as a
93 photocatalyst for pollutant degradation and hydrogen evolution, which owns good stability and
94 strong light absorption capability with a narrow bandgap of Eg ~ 2.11eV [17]. However, high
95 electron-hole recombination rate has seriously hindered its practical application. Xing *et al.* prepared
96 $In_2S_3@g-C_3N_4$ heterojunctions, which showed stronger photocatalytic activity in the degradation
97 of Rhodamine B (RhB) [18]. He *et al.* reported the synthesis of $In_2S_3@Bi_2WO_6$ core-shell
98 heterojunctions, in which the core-shell structure is conducive to the enhancement of the catalytic
99 activity of the photocatalyst [19].

100 In this paper, direct Z-scheme heterojunctions between $BiYWO_6$ and In_2S_3 were introduced
101 to inhibit the direct recombination of photogenerated carriers inside In_2S_3 and furtherly promote
102 the separation of the carriers, which results in the significant enhancement of the photocatalytic
103 activity. Experimental results and analysis show that In_2S_3 @ $BiYWO_6$ heterostructure
104 photocatalysts exhibit extremely excellent photocatalytic performance in comparison with
105 single-component photocatalysts. For example, the photocatalytic performance of 10IS-BYW (In_2S_3 :

BiYWO$_6$ = 10:1) was 2.46 times higher than that of In_2S_3 and 7.55 times higher than that of $BiYWO_6$, respectively. The formation and existence of $\bullet OH$ and $O_2^{\bullet-}$ radicals determined by radical species trapping experiments and fluorescence detection has confirmed that direct Z-scheme heterojunctions are indeed formed in the composite photocatalysts of $In_2S_3@BiYWO_6$. In addition, the composite photocatalysts with higher concentration of In_2S_3 exhibited extremely low adsorption rates towards Tetracycline Hydrochloride, revealing that the pollutions are most likely to be degraded through the photocatalysis instead of the adsorption. It efficiently overcomes the drawbacks of high adsorption rate and low photocatalytic degradation efficiency of pure $BiYWO_6$.

2. Experimental

2.1 Materials and reagents

All the chemical reagents used in the experiments were of analytical grade without any purification. Among them, Tetracycline Hydrochloride (TC-HCl), Rhodamine B (RhB), Methyl Blue (MB) and Malachite Green (MG) were purchased from ALADDIN (China) and the others were purchased from RHAWN (China).

2.2 Synthesis of $BiYWO_6$ photocatalysts

In a typical synthesis process, as shown in Fig. 1(a), 0.8 mmol of $Bi(NO_3)_3 \cdot 5H_2O$ and 0.8 mmol of $Y(NO_3)_3 \cdot 6H_2O$ were dissolved in 48 ml aqueous solution of HNO_3 (0.5 M) and heated up to 65 °C forming a transparent solution, designated as solution A. Solution B was made by dissolving 0.96 mmol of $Na_2WO_4 \cdot 2H_2O$ in 32 ml of 1 M NaOH aqueous solution. Then, solution A was added dropwise to solution B under vigorous stirring, and the mixture would gradually take on a milky color. After stirring for 30 min at room temperature, the pH of the mixed solution was kept at 13. At this time, HNO_3 was added dropwise to adjust the pH value to 9. The final solution was transferred to a PTFE lined 100 ml autoclave, which was heated under autogenous pressure and kept at 170 °C for 14 h. After cooling down to room temperature, the resulting sample was washed

several times with deionized water and ethanol and dried at 60 °C overnight. The obtained light-yellow powder was termed as $BiYWO_6$.

2.3 Synthesis of $In_2S_3@BiYWO_6$ composite photocatalysts

A simple two-step hydrothermal method was used to synthesize $In_2S_3@BiYWO_6$ composite photocatalysts. As shown in Fig. 1(b), 1 mmol of $InCl_3 \cdot 4H_2O$, 2 mmol of thioacetamide (TAA), 100 mg of urea, and different masses of $BiYWO_6$ were weighed and dissolved in 80 ml distilled water, and then stirred at room temperature for 30 min before transferring into a PTFE-lined 100 ml autoclave, which was heated to 180 °C and kept under autogenous pressure for 12 hours. After natural cooling to room temperature, the resulting sample was washed several times with distilled water and ethanol and dried at 60 °C overnight. $In_2S_3@BiYWO_6$ composite photocatalysts with different mass ratios (In_2S_3:$BiYWO_6$=1:2, 1:1, 5:1, 10:1, 20:1, and 30:1) were synthesized and labelled as IS-2BYW, IS-BYW, 5IS-BYW, 10IS-BYW, 20IS-BYW, and 30IS-BYW, respectively. In addition, a typical synthesis process for pure In_2S_3 was also shown in Fig. S6(a), and as-prepared sample presented dark yellow.

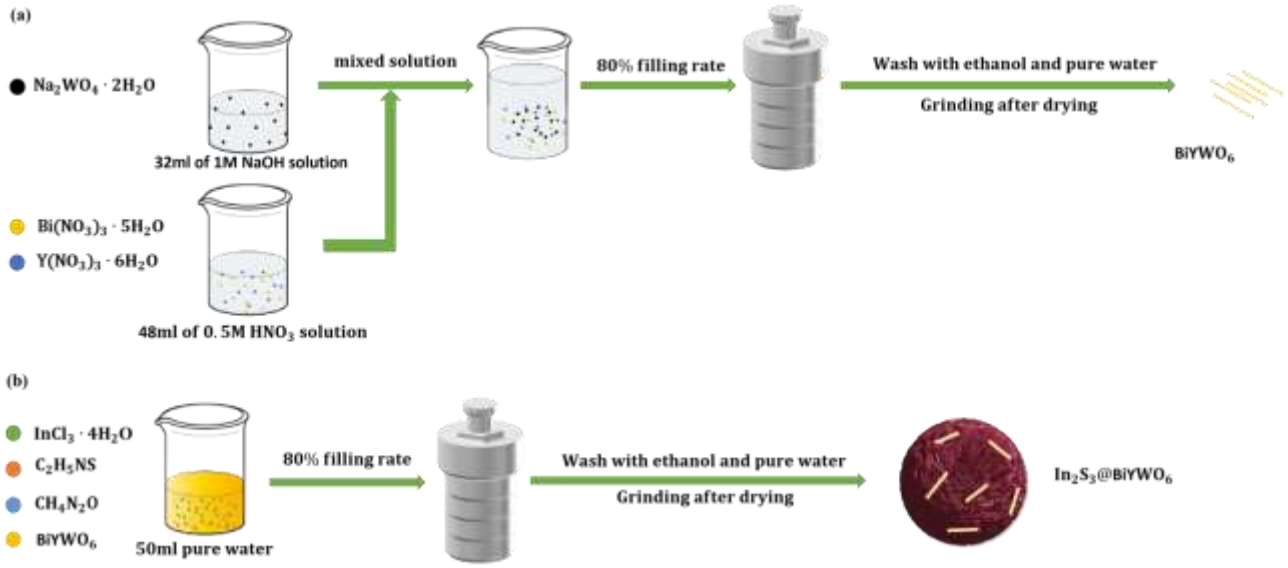

Figure 1 *Synthesis flowchart of (a)* $BiYWO_6$ *and (b)* $In_2S_3@BiYWO_6$

147 **2.4 Characterizations**

148 Powder X-ray diffraction (XRD) was performed on an X-ray diffractometer (D8 ADVANCEX)
149 to characterize the phase purity and crystalline structure of the samples. Morphological and
150 elemental profiles of the samples were observed by Scanning Electron Microscopy (Gemini SEM
151 500). Absorption profiles of pollutant solutions and powders were measured and recorded on a
152 UV-visible spectrometer (UV-2600). X-ray Photoelectron Spectroscopy (XPS, AXIS Ultrabld) was
153 employed to reveal the chemical states of all elements on the surface of the samples. Steady-state
154 photoluminescence (PL) emission spectra and time-resolved photoluminescence decay (TRPD)
155 spectra (excitation wavelength of 360 nm and emission wavelength of 425 nm) were measured on a
156 FLS-980 fluorescence spectrophotometer at room temperature.

157 **2.5 Photocatalytic activity measurements**

158 Photocatalytic activity of as-prepared samples was evaluated by degrading typical pollutants
159 such as Tetracycline Hydrochloride (TC-HCl), Rhodamine B(RhB), Methyl Blue (MB) and
160 Malachite Green (MG) in aqueous solution under visible light irradiation using a 500W Xe lamp
161 with a cutoff filter (λ > 420nm). In order to avoid the thermal catalytic effect caused by the
162 exothermic emission of Xe lamp, the system temperature was maintained at room temperature by a
163 cooling system. In a typical photocatalytic experiment, the photocatalyst (25 mg) was mixed with
164 0.02 mmol/L of 50 ml of pollutant aqueous solution to form a suspension in a reaction tube under
165 continuous stirring. Degradation of the pollutants was assessed by centrifuging the residual
166 photocatalyst powder every 5 min and recording the intensity of the absorption peak of the pollutant
167 to be degraded relative to its initial intensity (C/C_0).

168 **2.6 Radical species trapping and fluorescence detection measurements**

169 In order to reveal the charge transfer pathway in the heterojunction photocatalysts of
170 $In_2S_3@BiYWO_6$ (either Z-scheme or Type-II heterojunctions), radical species trapping experiments
171 and fluorescence detection of hydroxyl radicals ($\bullet OH$) were carried out in this work.

In the radical species trapping experiments, in order to determine which dominant radicals are mainly involved in the photocatalytic decomposition of pollutants, different trapping agents were used to evaluate the contribution of each radical. L-ascorbic acid (LAA), isopropanol (IPA) and sodium oxalate ($Na_2C_2O_4$) were used as the trapping agents for $O_2^{\bullet-}$, $\bullet OH$ and h^+, respectively. In the experiments, chemical probe compounds with high-rate reaction constants (k) are generally chosen as trapping agents. For example, L-ascorbic acid (LAA) was used as a trapping agent for $O_2^{\bullet-}$ with a reaction rate constant ($k[O_2^{\cdot-}]\sim3.4\times10^5M^{-1}s^{-1}$) [20, 21], and isopropanol (IPA) was used as a trapping agent for $\bullet OH$ with a reaction rate constant ($k[\bullet OH]\sim1.9\times10^9M^{-1}s^{-1}$) [22,23]. The concentration of all trapping agents in aqueous solution was to be kept at 1.0 mmol/L [11,24].

In the fluorescence detection of hydroxyl radicals ($\bullet OH$), photoluminescence (PL) spectra were employed to evaluate the yield rate of $\bullet OH$, usually using Terephthalic Acid (TA) as the probe molecule. During the photocatalytic reaction, some hydroxyl radicals ($\bullet OH$) are produced on the surface of the photocatalyst, and TA reacts with $\bullet OH$ to form 2- hydroxyterephthalic acid (TA-OH). Therefore, the amount of TA-OH is proportional to the amount of $\bullet OH$ [25,26]. In a typical run, 1L of NaOH solution ($2\times10^{-3}mol/L$) was firstly configured, and 5×10^{-4} mol of TA was dissolved into the NaOH solution; Finally, 25 mg photocatalyst was added into 50 ml of the above mixed solution. Under the visible light irradiation, sampling was performed every 10 min, and TA-OH in the solution was collected to determine the PL spectra. TA-OH is a highly fluorescent organic substance that emits a characteristic PL peak under light excitation, and the concentration of $\bullet OH$ radicals produced in the solution can be reflected by the PL intensity of TA-OH.

3 Results and Discussion

3.1 Structure Characterization

XRD patterns of all the samples are shown in Fig. 2. It is obvious that both In_2S_3 and $BiYWO_6$ samples have good crystallinity due to the sharp diffraction peaks. For pure In_2S_3, its

diffraction peaks of 14.0°, 27.5°, 33.4°, 43.8° and 47.9° correspond to (111), (311), (400), (511) and (440) diffraction planes respectively, based on the standard card (JCPDS No. 65-0459). For $BiYWO_6$, its diffraction peaks of 24.4°, 27.3°, 28.5°, 29.4° and 32.5° correspond to (120), (202), (-402), (320) and (-122) diffraction planes respectively, based on the standard card (JCPDS No. 33-0224). For the heterojunction composites, XRD patterns clearly show that the mixed diffraction peaks of In_2S_3 and $BiYWO_6$ present in the composites, and the diffraction peak intensities of the main peaks changes along with the change in the mass ratio of In_2S_3 and $BiYWO_6$. For instance, as the content of In_2S_3 increases, the diffraction peak (-402) intensity of $BiYWO_6$ gradually decreases, while the diffraction peak (440) intensity of In_2S_3 rapidly increases. In short, XRD results confirmed that both In_2S_3 and $BiYWO_6$ indeed co-existed in the composite photocatalysts, and no any impure phase was observed in all samples[27].

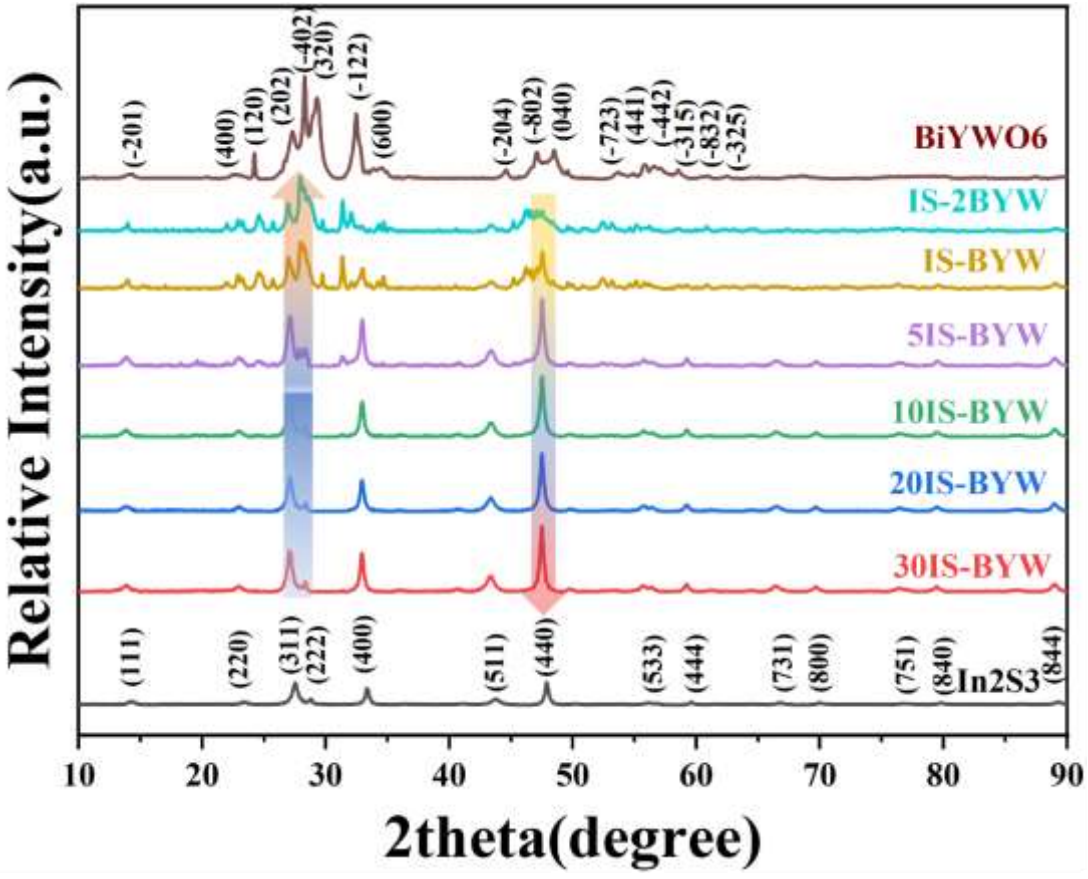

Figure 2 *XRD patterns of* In_2S_3, $BiYWO_6$ *and* $In_2S_3@BiYWO_6$

3.2 Morphology and element mapping analysis

Microstructure and morphologies of In_2S_3, $BiYWO_6$ and $In_2S_3@BiYWO_6$ photocatalysts were observed by Scanning Electron Microscope (SEM). SEM image of In_2S_3 (Fig. 3a) shows sphere-like aggregates with an average size of about 2μm, which is composed of many nano-sheets with thickness about 10nm. Figure 3b reveals the morphology of $BiYWO_6$ as nanorods with the diameter of 80~100nm. Concerning the morphologies of $In_2S_3@BiYWO_6$ composites (*i.e.* 5IS-BYW) as shown in Fig. 3c, the stacking of nanosheets in the sphere-like aggregates appears to be more tightly packed in comparison with Fig. 3a, which is due to the fact that the nanorods are embedded in the nanosheets. It is obvious that the sphere-like aggregates correspond to In_2S_3, while the nanorods for $BiYWO_6$ in the composites. Meanwhile, the homogeneous attachment of $BiYWO_6$ on In_2S_3 shows heterogeneous structure characteristics, which can lead to the formation of more active sites between the two materials enhancing the catalytic ability of the composites.

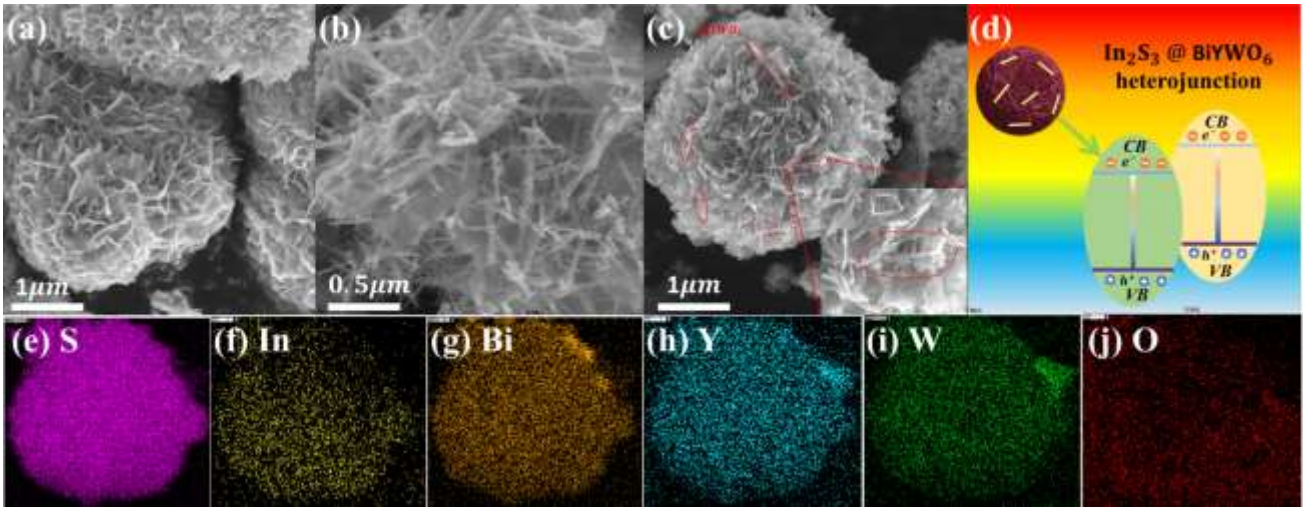

Figure 3 *Microstructure and morphologies of (a) In_2S_3, (b) $BiYWO_6$, (c) 5IS-BYW photocatalysts, (d) schematic diagram of the composite photocatalyst showing the formation of heterojunctions, (e-j) EDS Elemental Mapping analysis of 5IS-BYW.*

Meanwhile, in order to determine the elemental distribution in the composites, EDS elemental

Mapping analysis was carried out on the heterojunction photocatalyst of 5IS-BYW. As shown in Figs. 3e-j, the elements of In, S, Bi, Y, W, and O were observed in the heterojunction composite, which suggests the coexistence of In_2S_3 and $BiYWO_6$ in the composite. EDS mapping of In and S elements reflects clear spherical contours as shown in Figs. 3e&f, which are well consistent with the sphere-like aggregate of In_2S_3. As shown in Figs.3g-j, EDS mapping images of Bi, Y, W, and O elements show the uniform distribution of these elements in the spherical range, which further illustrates the composition of $In_2S_3@BiYWO_6$ heterojunctions. In brief, heterojunctions between In_2S_3 and $BiYWO_6$ were indeed formed in the composites. However, it is not yet possible to determine the charge transfer pathway in the heterojunctions (Z-scheme or Type-II mechanism), which will be discussed in the subsequent experiments.

Figure 4 shows XPS spectra of In_2S_3, $BiYWO_6$, and $In_2S_3@BiYWO_6$ (5IS-BYW) photocatalysts. From the survey spectra (Fig. 4a), it can be seen that pure In_2S_3 contains the elements of S and In, while $BiYWO_6$ contains the elements of Bi, Y, W, and O. As expected, $In_2S_3@BiYWO_6$ (5IS-BYW) composite consist of S, In, Bi, Y, W and O elements. The coexistence of S, Y and Bi elements in the composite will interfere with each other. At the same time, the XPS peaks of Y and Bi elements almost overlap. Therefore, the high-resolution XPS spectra of S, Y and Bi were analyzed in a single figure (Fig. 4b). The high-resolution XPS spectra of Y 3d and Bi 4f show two main peaks at 163.9eV and 158.6eV, respectively, which are associated with $3d_{5/2}$ and $3d_{3/2}$ of Y^{3+}, concurrently corresponding to $4f_{7/2}$ and $4f_{5/2}$ of Bi^{3+} [28]. Some distortion was produced on the shoulder of $Bi\ 4f_{7/2}$ and $4f_{5/2}$ by comparing the XPS spectra of Bi^{3+} in $BiYWO_6$, and $In_2S_3@BiYWO_6$ $(5IS-BYW)$, which should be attributed to the formation of heterojunctions in the composite material [29]. Typically, two peaks of S 2p appear at 161.2 and 162.5eV, corresponding to $2p_{3/2}$ and $2p_{1/2}$ of S^{2-}, respectively (Fig. 4b) [30]. The presence of two W 4f peaks at 35.87 eV ($4f_{7/2}$) and 38.01 eV ($4f_{5/2}$) indicates that tungsten is presented in W^{6+}(Fig. 4d). The 3d core splits of In for $In_2S_3@BiYWO_6$ were $3d_{5/2}$ (444.90 eV) and

$3d_{3/2}$(452.45 eV), being consistent with the value of In^{3+}(Fig. 4e). The fine spectral data for each element can be seen in Table S1.

XPS spectra of O1s for $BiYWO_6$ and $In_2S_3@BiYWO_6$ (5IS-BYW) are shown in Fig.4c. Obviously, XPS spectrum of each O1s is not a unimodal curve, which should include three peaks corresponding to metal-oxygen bonds (such as Bi-O bonds and Y-O bonds in $BiYWO_6$), dangling bonds and surface-adsorbed bonds (their energies from low to high) [5]. In order to obtain the exact position of each peak, each curve is properly fitted on the basis of the Pseudo-Voigt fitting function. Generally, the two characteristic peaks of dangling bonds and adsorbed oxygen are suggested as the typical characteristics of oxygen vacancies presented in the oxides. In addition, the concentration of oxygen vacancies can be indirectly estimated by the relative peak intensity ratios ($R_{peaks}=(I_{DL}+I_{ADS})/I_{M\text{-}O}$) between metal-oxygen bonds (*M-O*) and the sum of dangling bonds (*DL*) and adsorbed oxygen (*ADS*) [5]. R_{peaks} of $BiYWO_6$ and $In_2S_3@BiYWO_6$ (5IS-BYW) are 1.12 and 0.76 respectively, which means that the concentration of oxygen vacancies in the composite of $In_2S_3@BiYWO_6$ (5IS-BYW) is much lower than that in pure $BiYWO_6$. It is known that oxygen vacancies are positively charged. The large reduction of oxygen vacancies in the composite of $In_2S_3@BiYWO_6$ (5IS-BYW) compared to pure $BiYWO_6$ means that negative electrons transfer from In_2S_3 to $BiYWO_6$ through the interface. As a result, a built-in electric field (E_i) is formed at the interface pointing from In_2S_3 to $BiYWO_6$ when the electron flow reaches equilibrium. Once the photogenerated carriers are excited in both In_2S_3 and $BiYWO_6$, this built-in electric field will drive the photogenerated electrons on the CB of $BiYWO_6$ recombine with the holes on the VB of In_2S_3, instead of photogenerated electrons transfer from the CB of In_2S_3 to the CB of $BiYWO_6$. Obviously, this is typical characteristic of the Z-scheme charge transfer (as shown in Fig.9).

In addition, it is noteworthy that both O 1s and W 4f characteristic peaks of $BiYWO_6$ component slightly shift to higher binding energies upon formation of heterojunctions with In_2S_3 compared to pure $BiYWO_6$ (Fig. 4c and d), whereas S 2p of $In_2S_3@BiYWO_6$ slightly shifted to a

lower binding energy (Fig. 4b). It should be also attributed to the transfer of some electrons from S of In_2S_3 to O of $BiYWO_6$, which further verifies the Z-scheme charge transfer mechanism in the heterojunctions of $In_2S_3@BiYWO_6$. In a word, XPS results indicate that In_2S_3 and $BiYWO_6$ coexist in the composites and the charge transfer pathway in the heterojunction favors the Z-scheme mechanism [31].

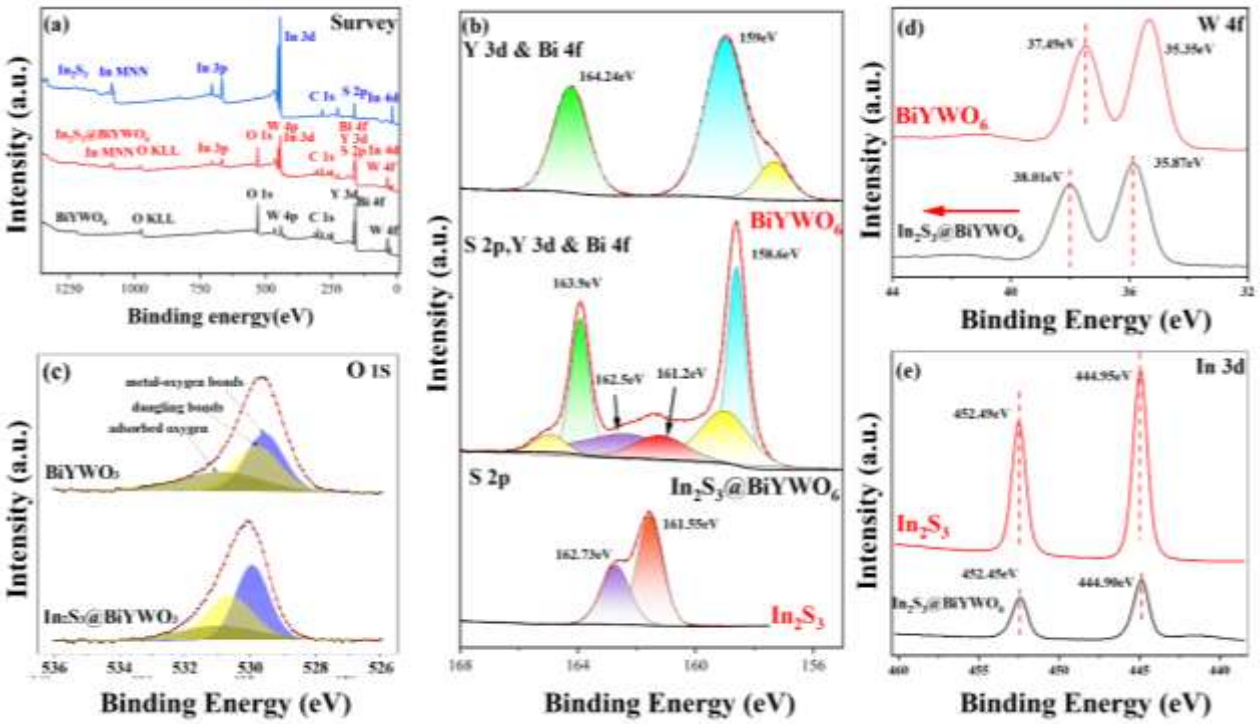

Figure 4. *(a) XPS survey spectra and high-resolution XPS of (b) S2p, Y3d& Bi4f, (c)O1s, (d) W4f and (e) In3d in* In_2S_3, $BiYWO_6$, *and* $In_2S_3@BiYWO_6$ *composite*

3.3 Photocatalytic activities of $In_2S_3@BiYWO_6$ composites

In this work, the photocatalytic performance of the photocatalysts was mainly evaluated by degrading tetracycline hydrochloride (TC-HCl) under visible light irradiation. Usually, organic molecules in the pollutant solution will be physically adsorbed on the surface of the photocatalyst for a certain period of time, which suggests that the physical adsorption also affects the evaluation of the catalytic performance of the photocatalyst [32]. In order to accurately evaluate the photocatalytic performance, each photo-degradation reaction was carried out in adsorption equilibrium for 60 min

before irradiation. As shown in Fig. 5(a), pure In_2S_3 shows a moderate photocatalytic degradation ability (only 54% of the pollutants decomposed after 30 min irradiation) due to its fast electron-hole recombination. Pure $BiYWO_6$ owns a high physical adsorption rate of 50%, and its superficial catalytic performance was slightly better than that of pure In_2S_3 (63% of the pollutants decomposed after 30 min irradiation). However, the high physical adsorption rate of $BiYWO_6$ reduces its practicability and stability. In order to overcome this problem, the low physical adsorption rate of In_2S_3 was introduced and formed the composites with $BiYWO_6$. Interestingly, 10IS-BYW composite can decompose up to 85% of the pollutants after 30 min irradiation, exhibiting an excellent photocatalytic performance.

In order to more accurately assess the catalytic ability of the catalysts, a quasi-first-order kinetic model was fitted to the reaction kinetic parameters of the different composites for the degradation of tetracycline hydrochloride [32,33].

$$\ln(C_0/C) = kt + c \quad (1)$$

where C_0/C represents the photocatalytic efficiency (ratio of initial concentration of pollutant to the concentration after a certain interval) and k is the quasi-first-order reaction rate constant.

After performing the kinetic fitting, the k value can be estimated from the slope of the fitted curve of $\ln(C_0/C)$ *versus* time as shown in Fig. 5b. Figure 5c shows the k-values corresponding to different photocatalysts, which are basically in agreement with the catalytic ability reflected in Fig. 5(a). The k-value of 10IS-BYW sample was as the highest as $0.06263\ min^{-1}$ reflecting the best photocatalytic activity, which was 2.46 and 7.55 times higher than that of pure In_2S_3 and $BiYWO_6$, respectively. The k-values of the other composites were also in accordance with the catalytic ability reflected in Fig. 5(a), which indicates that the quasi-first-order kinetic model was completely applicable to the degradation of tetracycline hydrochloride by the photocatalysts. Concerning pure $BiYWO_6$, its k value is lower than that of pure In_2S_3, although its superficial catalytic performance

was slightly better than that of pure In_2S_3. This also just shows that the high adsorption capacity of $BiYWO_6$ is not entirely beneficial to its photocatalytic performance. Among all the composite samples, the photocatalytic ability of the sample highly doped with $BiYWO_3$ (such as IS-2BYW) is lower than that of the two single-component catalysts. Probably, too many $BiYWO_6$ nanorods agglomerate on the surface of In_2S_3 spheres, leading to the reduction of the specific surface area of the composite material and shielding the active sites.

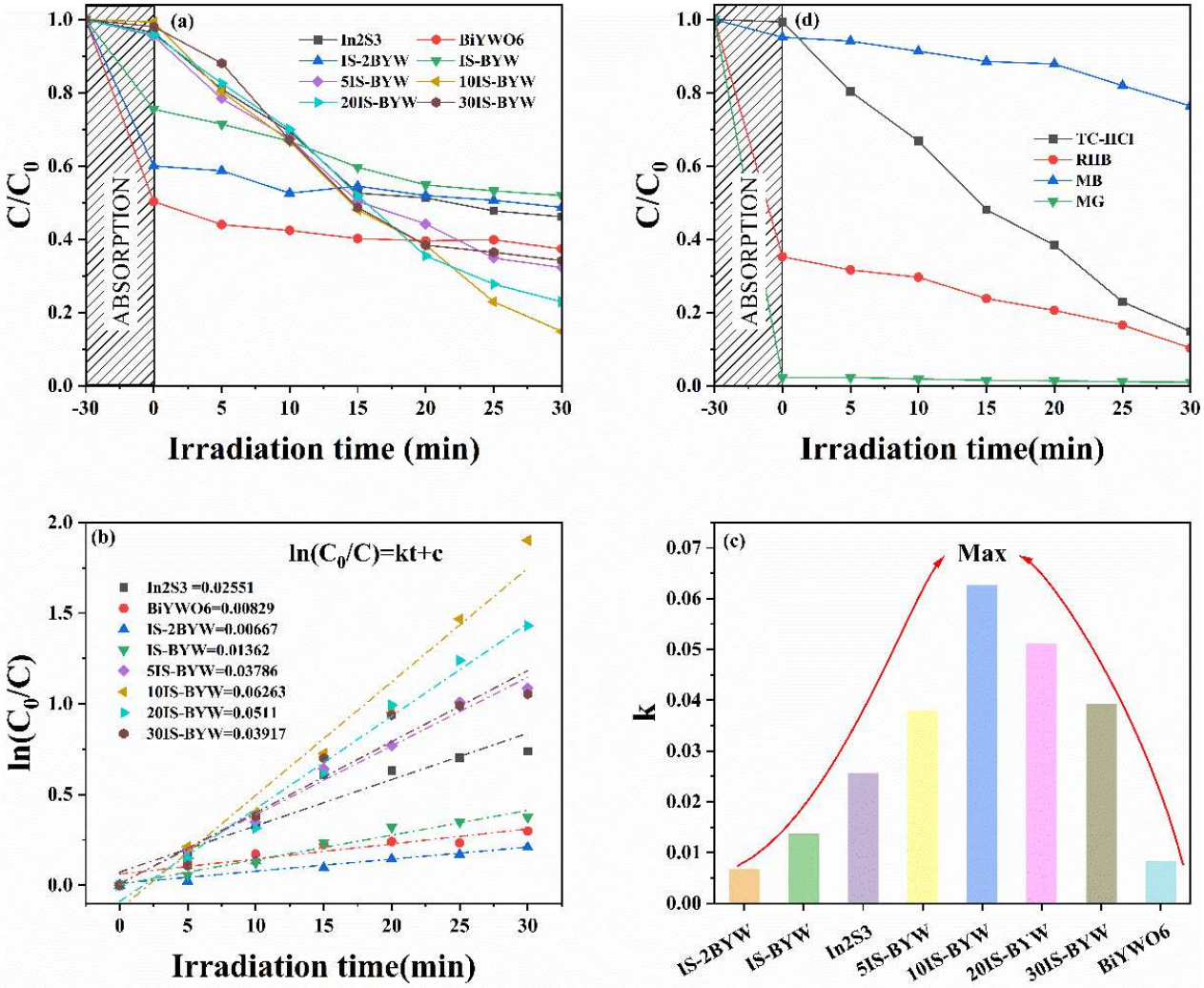

Figure 5 *(a) Photocatalytic decomposition efficiency (C/C_0) of tetracycline hydrochloride by photocatalysts, (b) Kinetic fitting of the photocatalytic reaction, (c) Estimated kinetic k values, and (d) Photocatalytic degradation efficiencies (C/C_0) towards TC-HCl, RhB, MB, and MG*

Figure 5(d) shows the photocatalytic activities of $In_2S_3@BiYWO_6$ (10IS-BYW) towards the

decomposition of four different micropollutants, such as Rhodamine B (RhB), Methylene Blue (MB), Tetracycline Hydrochloride (TC-HCl) and Malachite Green (MG). Apparently, the composite photocatalyst had different degradation abilities towards different organic pollutants, with the best degradation ability towards TC-HCl and the worst towards MB.

Detailed degradation efficiencies of different micropollutants are summarized in Table 1. The photocatalytic degradation efficiency of organics may be closely related to their molecular structures, since different energies are required to break and restructure the chemical bonds in different organic molecules. Apparently, Methyl Blue (MB) has a more complex molecular structure than Rhodamine B(RhB) and Malachite Green (MG), which therefore requires more energy for decomposition [34]. In addition, the type of chemical bonding may also influence the photocatalytic efficiency; for example, MB molecule contains S-O bonds, which makes it more difficult to be oxidized [35, 36]. For MG, about 97% of it has been physically adsorbed by 10IS-BYW at the adsorption equilibrium, which is mainly related to the strong adsorption of $BiYWO_6$.

Table 1 Characterization and degradation efficiencies of different micropollutants

Category	Pollutants	Molecular formula	Molecular weight (g/mol)	Removal efficiency (After 30 min irradiation)	k value (cm^{-1})
Antibiotics	Tetracycline hydrochloride (TC-HCl)	$C_{22}H_{25}ClN_2O_8$	480.90	85.16	**0.06263**
Dyes	Rhodamine B (RHB)	$C_{28}H_{31}ClN_2O_3$	479.01	89.71	**0.03822**
	Methylene blue (MB)	$C_{37}H_{27}N_3Na_2O_9S_3$	799.80	23.61	**0.00696**
	Malachite green (MG)	$C_{23}H_{25}ClN_2$	346.47	99.08	**0.03242**

It is known that the initial pH of the solution also impacts the photocatalytic ability of the photocatalyst. The pH value of solution not only affects the charge transfer on the surface of the photocatalyst, but also leads to the ionization of the organic pollutants in the solution [37]. Therefore, in this paper, effect of pH value on the photocatalytic activity of $In_2S_3@BiYWO_6$ composite catalysts were also investigated by degrading tetracycline hydrochloride. As shown in Fig. 6(a), the

degradation efficiency increases from 69.7% to 85.16% as pH value of the solution increases from 3.5 to 6.5, while the degradation efficiency drops dramatically to 26.76% as the pH value gradually increases to 10. It is believed that the reaction of h^+ with Cl^{-1} and $\bullet OH$ under acidic condition enhances the degradation efficiency of tetracycline hydrochloride [38]. On the contrary, the negative charges attached on the surface of the catalyst increase dramatically under alkaline condition leading to the formation of electrostatic repulsion between the catalyst and tetracycline hydrochloride, which was not conducive to the adsorption of the pollutant and the oxidation reaction. Overall, 10IS-BYW can effectively decompose tetracycline hydrochloride in the pH range of 3.5-6.5, owning the excellent photocatalytic activity in the acidic solutions.

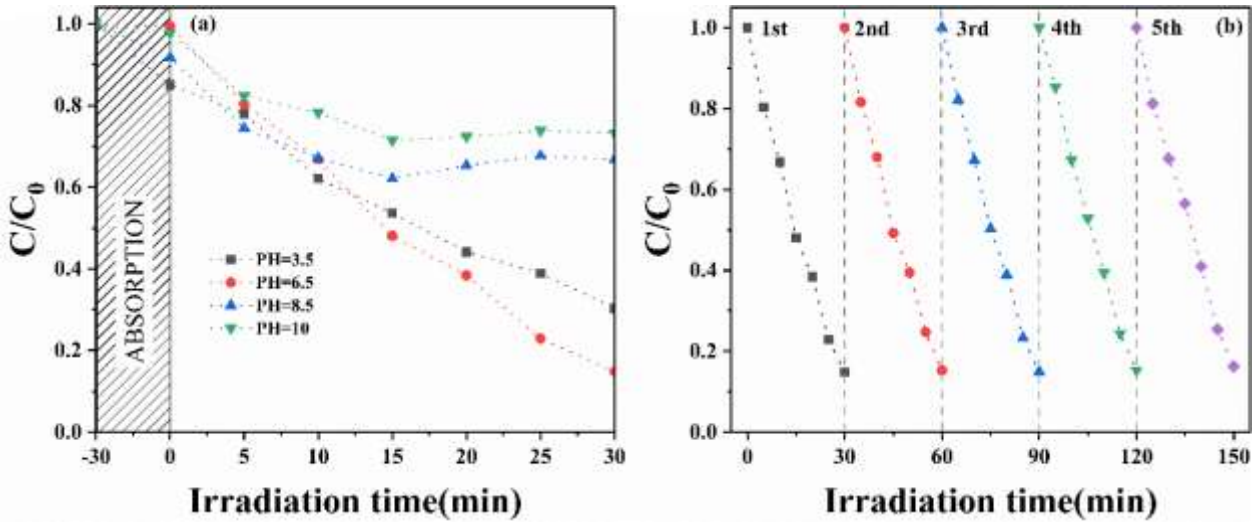

Figure 6 *(a) pH effect on the photocatalytic activity of 10IS-BYW, (b) cycling experiment*

In order to investigate the stability and reusability of $In_2S_3@BiYWO_6$ composite catalysts, five photocatalytic cyclic experiments on the sample of 10IS-BYW were carried out in this paper (using tetracycline hydrochloride as the target pollutant). The photo-degradation efficiencies from the first to the fifth times were 85.16%, 84.71%, 85.08%, 84.7%, 83.78%, and 83.78%, respectively, without obvious change. Therefore, $In_2S_3@BiYWO_6$ photocatalysts have good stability and

362 reusable value, which provides a good reference for its practical application.

363 **3.4 Determination of the dominant radical species in the photocatalytic reaction**

364 In order to determine the active radicals in the degradation of organic matter by the
365 photocatalysts, three radical trapping agents of L-ascorbic acid (LAA), isopropanol (IPA), and
366 sodium oxalate ($Na_2C_2O_4$) were used to quench superoxide radicals ($O_2^{\bullet-}$), hydroxyl radicals ($\bullet OH$),
367 and photogenerated holes (h^+), respectively. As shown in Fig. 7a~d, the degradation of tetracycline
368 hydrochloride by pure $BiYWO_6$ was obviously inhibited by $Na_2C_2O_4$, whereas the degradation
369 efficiency of pure In_2S_3 decreased dramatically due to adding LAA. It suggests that $O_2^{\bullet-}$ and h^+
370 correspond to the major radical species for the degradation of tetracycline hydrochloride by In_2S_3
371 and $BiYWO_6$, respectively.

372 As far as the quenching experiment of 10IS-BYW are concerned (Fig. 7e&f), both L-ascorbic
373 acid and sodium oxalate significantly inhibited the degradation of tetracycline hydrochloride. The
374 results show that $O_2^{\bullet-}$ and h^+ are the main radicals for the decomposition of tetracycline
375 hydrochloride by the composite catalysts, as well as minor effect from $\bullet OH$. Apparently, $O_2^{\bullet-}$ is
376 mainly contributed by In_2S_3, while h^+ or $\bullet OH$ is contributed by $BiYWO_6$. The experimental
377 results show that the redox capacity of 10IS-BYW is much higher than that of In_2S_3 and $BiYWO_6$.
378 In other words, more photogenerated electrons are concentrated in the CB of In_2S_3, and more
379 photogenerated holes are concentrated in the VB of $BiYWO_6$, which is exactly in accordance with
380 the Z-scheme heterostructure instead of traditional Type-II heterostructure.

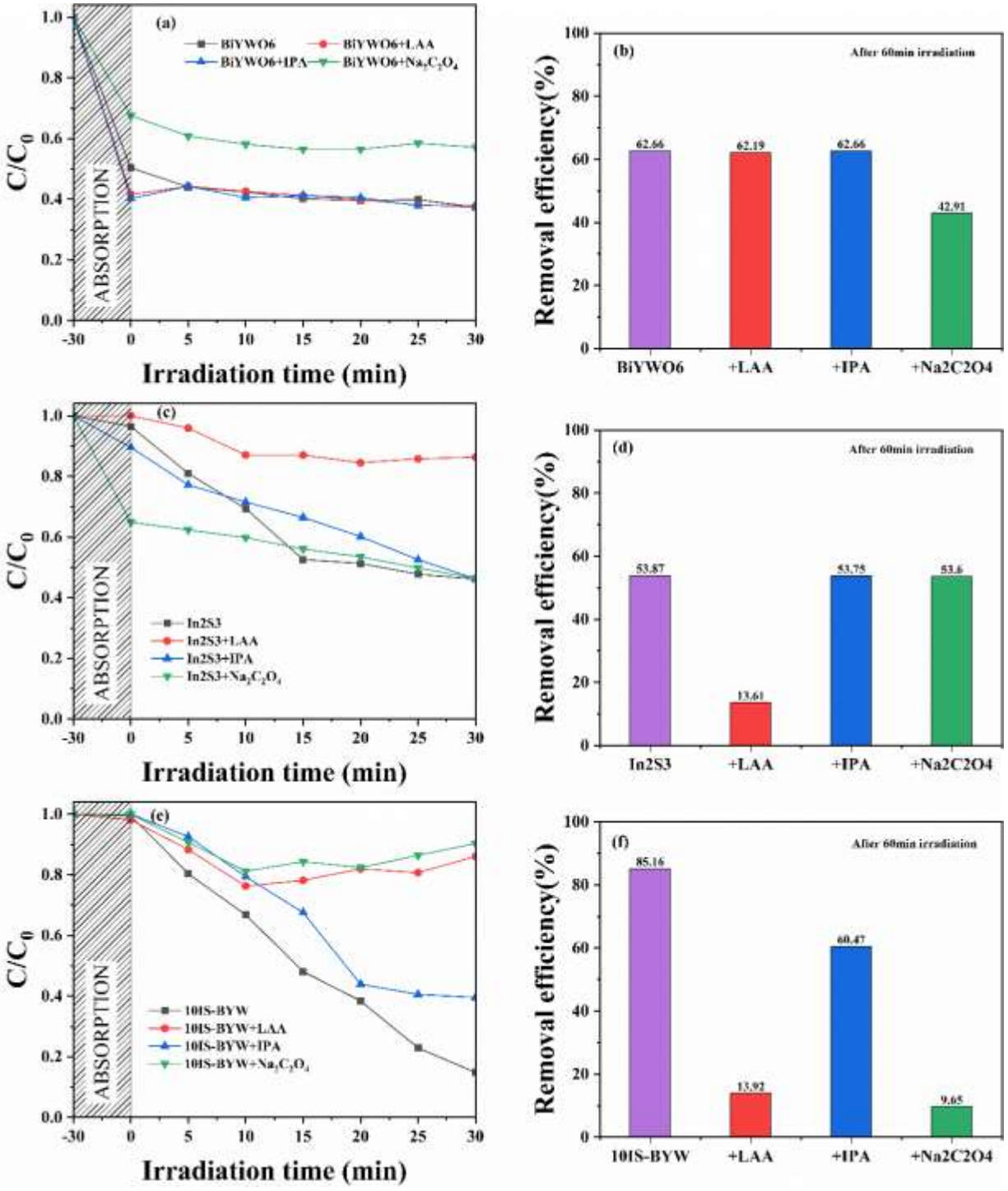

Figure 7 *Radical species trapping experiments of (a)&(b) pure* $BiYWO_6$*, (c)&(d) pure* In_2S_3 *and (e)&(f) 10IS-BYW heterojunctions*

In addition, photoluminescence (PL) spectroscopy was also used to further investigate the charge separation and transfer pathway in $In_2S_3@BiYWO_6$ composites. Terephthalic Acid (TA) react with ·OH to produce highly fluorescent 2-Hydroxyterephthalic Acid (TA-OH) with a

387 characteristic PL peak around 425nm as shown in Fig. 8(c). As shown in Fig. 8(a)&(b), the
388 fluorescence signals of TA-OH can be clearly observed for both $BiYWO_6$ and $In_2S_3@BiYWO_6$
389 composites, while almost no signal for pure In_2S_3. It suggests that $\bullet OH$ radicals can be produced
390 by both $BiYWO_6$ and $In_2S_3@BiYWO_6$ composites, instead of In_2S_3. Furthermore, the emission
391 peaks intensities of $In_2S_3@BiYWO_6$ composites are significantly enhanced in comparison with
392 $BiYWO_6$, which indirectly reflect higher redox capacity of photogenerated holes in the VB of
393 $In_2S_3@BiYWO_6$ composites. In the composites of $In_2S_3@BiYWO_6$, electrons (e^-) in the VB of
394 both $BiYWO_6$ and In_2S_3 are excited into the CB, and holes (h^+) are left in their valence bands
395 under light irradiation. Subsequently, e^- in the CB of $BiYWO_6$ is recombined with h^+ in the VB
396 of In_2S_3 under the action of built-in electric field (*Ei*) in the interface of heterojunction, while
397 highly redox-active carriers (e^- in the CB of In_2S_3 and h^+ in the VB of $BiYWO_6$) are retained
398 and then more $\bullet OH$ radicals are produced by highly redox-active h^+ in the component of
399 $BiYWO_6$. Although 5IS-BYW produced the most $\bullet OH$ radicals, 10IS-BYW exhibited the strongest
400 photocatalytic activity. It should be mentioned that h^+ are the main radicals for the decomposition of
401 tetracycline hydrochloride by the composite photocatalysts (as shown in the radical species trapping
402 experiments), rather than $\bullet OH$. It suggests that 10IS-BYW produces much more holes relative to
403 5IS-BYW, and thus 10IS-BYW exhibits greater photocatalytic ability.

404 To further investigate the photogenerated charge separation efficiency of the composite
405 photocatalysts, the time-resolved photoluminescence decay (TRPD) spectra of pure $BiYWO_6$ and
406 5IS-BYW (Fig. 8(d)) were carried out. TRPD lifetimes were obtained by fitting the data with a
407 double-exponential equation ($\tau_{avg}=(A_1\tau_1^2 + A_2\tau_2^2)/(A_1\tau_1 + A_2\tau_2)$) [39]. Generally, the longer the
408 fluorescence lifetime of the catalyst, the more difficult it is for electrons and holes to recombine.
409 Table 2 shows that 5IS-BYW composite displays a longer average fluorescence lifetime ($\boldsymbol{\tau_{avg}}$ ~
410 7.61ns) than that of pure $BiYWO_6$ ($\boldsymbol{\tau_{avg}}$ ~ 6.82ns), revealing that the heterojunction formed in the
411 composites can significantly enhance the charge carrier separation efficiency. This is one of the main

reasons why the photocatalytic performance of In_2S_3@$BiYWO_6$ composite is superior to that of pristine In_2S_3 and $BiYWO_6$.

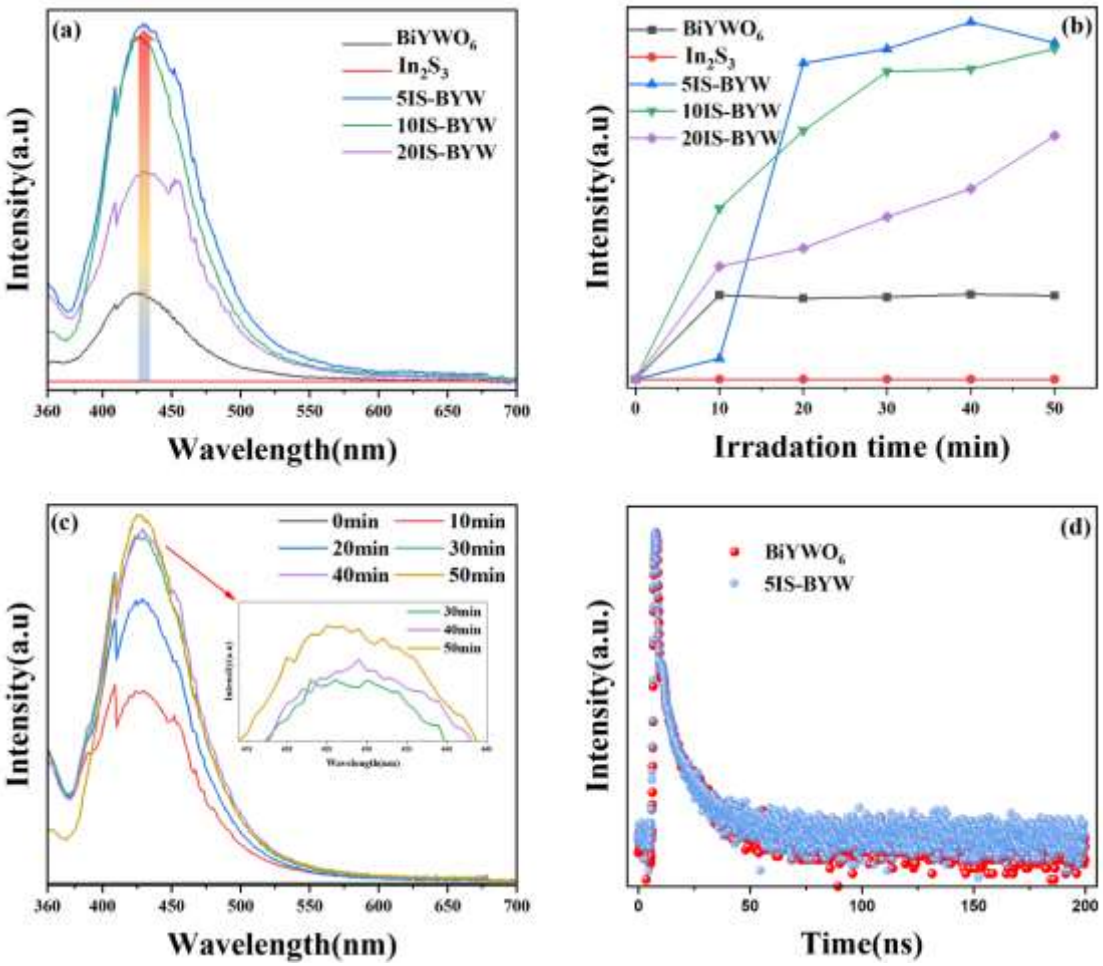

Figure 8 *(a) Photoluminescence spectra of TA-OH for different photocatalysts after irradiation for 50 min, (b) Temporal evolution of PL spectra of TA-OH for different photocatalysts, (c) PL intensity of TA-OH at 425nm versus irradiation time for 10IS-BYW,(d) time-resolved photoluminescence decay (TRPD) spectra of* $BiYWO_6$ *and 5IS-BYW.*

Table 2 The fitted TRPD lifetimes of the pure $BiYWO_6$ and 5IS-BYW composites.

Samples	A1(%)	τ_1(ns)	A2(%)	τ_2(ns)	τ_{avg}(ns)
$BiYWO_6$	35.5	1.20	64.5	7.33	6.82
5IS-BYW	31.75	1.34	68.25	8.09	7.61

3.5 Possible photocatalytic mechanism

In order to have a comprehensive understanding on the photocatalytic mechanism of $In_2S_3@BiYWO_6$ heterojunctions, the conduction band (CB) and valence band (VB) potentials of $In_2S_3@BiYWO_6$ composites have been estimated based on the concept of electronegativity in this work. CB and VB potentials of semiconductor can be calculated by the following equations [40]:

$$E_{VBM} = \chi - E^e + 0.5E_g \quad (2)$$

$$E_{CBM} = E_{VBM} - E_g \quad (3)$$

where E_g is the bandgap energy. χ is the Mulliken electronegativity of semiconductor. The estimated values of χ for In_2S_3 and $BiYWO_6$ are 4.70 and 6.05 eV, respectively [17, 28]. E^e is the free electron energy on the hydrogen scale (about 4.50 eV). As calculated from the UV-Vis diffuse reflectance spectra (Fig. S5) [41-43], E_g of In_2S_3 and $BiYWO_6$ are about 2.11 and 2.97eV, respectively. Therefore, E_{VBM}/E_{CBM} of In_2S_3 and $BiYWO_6$ are estimated as 1.26 /-0.86 eV and 3.03 /0.06 eV, respectively [44].

Based on the above discussions, charge transfer pathway or mechanism of $In_2S_3@BiYWO_6$ heterojunction can be profiled in more depth to determine whether it is a conventional Type-II heterojunction or a direct Z-scheme heterojunction. As shown in Fig. 9, although both Type-II and Z-scheme heterojunctions require the heterostructures with staggered energy bands, their charge transfer pathways are significantly different. As shown in Fig. 9a, for the conventional Type-II heterojunction, since E_{CBM} of In_2S_3 is higher than that of $BiYWO_6$ and E_{VBM} of $BiYWO_6$ is lower than that of In_2S_3, the photogenerated electrons are more preferred to transfer from the CB of In_2S_3 to the CB of $BiYWO_6$, while the photogenerated holes can easily be transferred from the VB of $BiYWO_6$ to the VB of In_2S_3. Such a charge transfer pathway will lead to reduction in the redox potential of photogenerated carriers. Moreover, E_{CBM} (0.06 eV) of $BiYWO_6$ is lower than the reduction potential of $O_2^{\bullet-}$ (-0.33 eV *vs NHE*), and E_{VBM} of In_2S_3 (1.26 eV) is higher than the

oxidation potential of $\bullet OH(\bullet OH/OH = 2.38eV,\ \bullet OH/H_2O = 2.72eV)$. Therefore, superoxide radicals ($O_2^{\bullet -}$) and hydroxyl radicals ($\bullet OH$) cannot be observed in the photocatalytic reactions of $In_2S_3@BiYWO_6$ composites if they are the conventional Type-II heterostructures, which contradicts previous experimental results. Obviously, charge transfer pathway in the composite photocatalysts of $In_2S_3@BiYWO_6$ prefers the direct Z-scheme mechanism, rather than the Type-II mechanism[45].

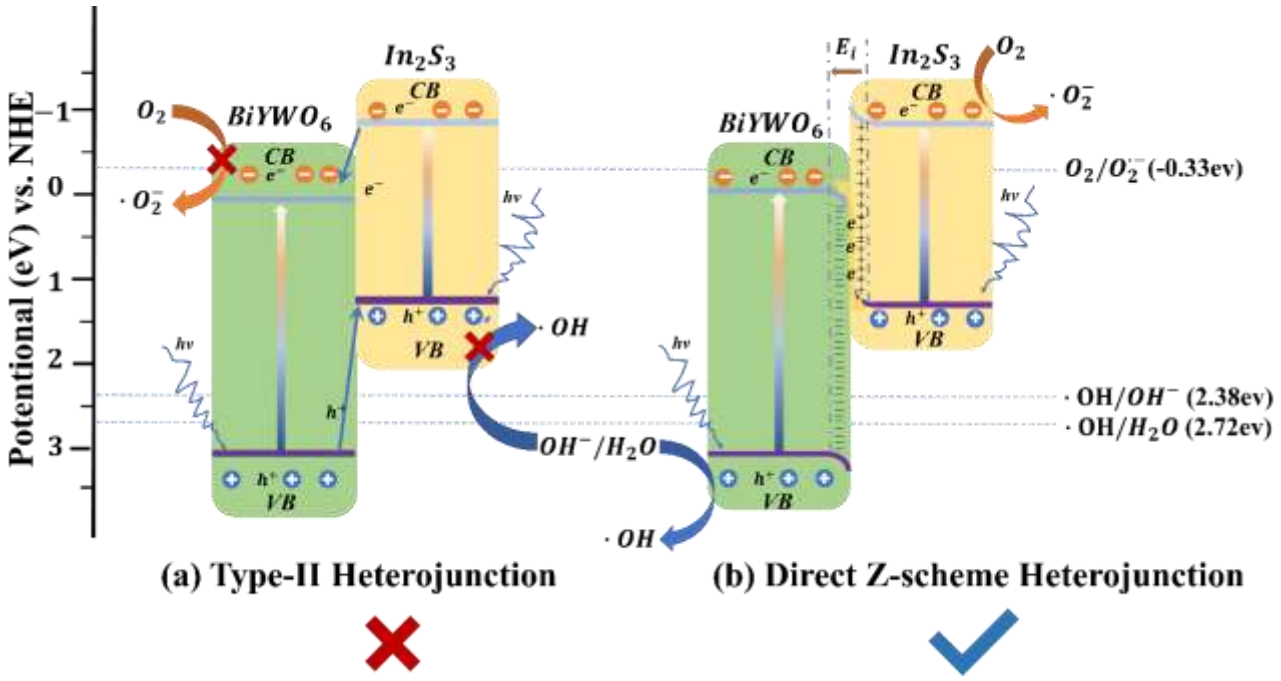

Figure 9 *Schematic diagram of charge transfer mechanisms in the heterojunction of $In_2S_3@BiYWO_6$ (a) Type-II, (b) direct Z-scheme*

Based on the above analysis and principal of the Z-scheme heterojunction, the following formulas are helpful to more clearly illustrate the intrinsic mechanism of the photocatalytic decomposition of tetracycline hydrochloride (TC-HCl) by $In_2S_3@BiYWO_6$ [40,41,46].

$$In_2S_3 + hv \rightarrow In_2S_3\ (h^+ + e^-) \quad (4)$$

$$BiYWO_6 + hv \rightarrow BiYWO_6\ (h^+ + e^-) \quad (5)$$

$$\boldsymbol{e^-}(BiYWO_6) + \boldsymbol{h^+}(In_2S_3) \rightarrow \mathbf{0}\ (Recombination) \quad (6)$$

$$O_2 + e^-(In_2S_3) \rightarrow O_2^{\bullet -} \quad (7)$$

$$TC - HCl + O_2^{\bullet -} \rightarrow Degraded\ products \quad (8)$$

$$TC - HCl + h^+(BiYWO_6) \rightarrow Degraded\ products \quad (9)$$

As two catalysts contact each other, their different Fermi energy levels result in electrons migration from In_2S_3 to $BiYWO_6$. As shown Fig. 9b, the key built-in electric field E_i will form at the contact interface between In_2S_3 and $BiYWO_6$, which has been confirmed by above XPS results. At the same time, both In_2S_3 and $BiYWO_6$ undergo energy band bending (Fig. 9b), until two Fermi energy levels converge. In this case, once the photogenerated carriers are generated in In_2S_3 and $BiYWO_6$ under the light irradiation, this built-in electric field E_i will drive the photogenerated electrons on the CB of $BiYWO_6$ to recombine with the holes on the VB of In_2S_3 (see formula 6). After a part of the photogenerated carriers undergoes recombination, the remaining photogenerated carriers will have stronger redox ability; *for instance*, photogenerated electrons retained on the CB of In_2S_3 has a stronger reduction potential (-0.86eV), which strongly reduces O_2 into the radicals of $O_2^{\bullet -}$ (-0.33eV) [42] (see formula 7). Meanwhile, photogenerated holes retained on the VB of $BiYWO_6$ has stronger oxidizing ability (3.03eV). These highly reactive radicals become the dominant radicals in the composite photocatalysts to efficiently oxidize organic pollutants (see formulas 8&9). In brief, the direct Z-scheme heterojunction formed between In_2S_3 and $BiYWO_6$ greatly improves the photocatalytic performance of the composites [39]. In addition, h^+ on the VB of $BiYWO_6$ (3.03eV) can oxidize OH^- or H_2O into the radicals of $\bullet OH$ ($\bullet OH/OH^- = 2.38eV$, $\bullet OH/H_2O = 2.72eV$) [47], which provides a minor contribution to the photodegradation of organic matter. Meanwhile, it is also evidence for the Z-scheme carrier transfer pathway or mechanism in the heterojunctions of $In_2S_3@BiYWO_6$ revealed by the fluorescence detection.

4. Conclusion

In conclusion, a simple two-step hydrothermal method was introduced herein to successfully synthesis the composite photocatalysts of $In_2S_3@BiYWO_6$ with high catalytic activity and good

483 stability, where $BiYWO_6$ nanorods were uniformly embedded on the surface of In_2S_3
484 microspheres to form a large number of heterojunctions. Based on the degradation experiments of
485 organic pollutants, it can be determined that the photocatalytic performance of the composite
486 photocatalysts is significantly improved in comparison with the single-component catalysts.
487 Especially, 10IS-BYW composite photocatalyst exhibits the highest photocatalytic efficiency, which
488 is 2.46 and 7.55 times higher than that of pure In_2S_3 and $BiYWO_6$, respectively. According to XPS
489 analysis, the radical species quenching experiment and PL spectra, charge transfer pathways in the
490 $In_2S_3@BiYWO_6$ heterojunctions are obviously more inclined to the Z-scheme mechanism, rather
491 than the traditional Type-II mechanism. The composite photocatalysts of $In_2S_3@BiYWO_6$ prepared
492 in this work enrich the Z-scheme heterojunction photocatalyst systems.
493

ACKNOWLEDGEMENTS

Financial support by the National Natural Science Foundation of China (Grant NO. 52072296) is gratefully acknowledged. The authors also acknowledge the financial support by National Key Laboratory of Science and Technology on Vacuum Technology and Physics, Lanzhou Institute of Physics, China.

Declaration of Competing Interest

The authors declare that they have no known competing financial interests or personal relationships that could have appeared to influence the work reported in this paper.

Data availability

Data will be made available on request.

CRediT authorship contribution statement

Junlong Zhang: Methodology, Investigation, Data curation, Writing – original draft. **Jie Wei**: Conceptualization, Project administration, Funding acquisition, Supervision, Writing – review & editing. **Minchuan Xiahou**: Investigation. **Zehao Sun**: Data curation. **Ao Cao**: Data curation. **Youxin Yuanfeng**: Data curation. **Yanchun He**: Funding acquisition. **Shigeng Song:** Supervision.

References

[1] M. Laqbaqbi, M.C. García-Payo, M. Khayet, J. El Kharraz, M. Chaouch, Application of direct contact me mbrane distillation for textile wastewater treatment and fouling study, Sep. Purif. Technol. 209 (2019) 815–825. https://doi.org/10.1016/j.seppur.2018.09.031.

[2] R. Daghrir, P. Drogui, Tetracycline antibiotics in the environment: a review, Environ. Chem. Lett. 11 (2013) 209–227. https://doi.org/10.1007/s10311-013-0404-8.

[3] M. Yu, C. Liu, X. Sun, J. Lu, J. Niu, Understanding of the Dual Roles of Phosphorus in Atomically Distributed Fe/Co-N4P2 over Carbon Nitride for Photocatalytic Debromination from Tetrabromobisphenol A, ACS Appl. Mater. Interfaces. 14 (2022) 5376–5383. https://doi.org/10.1021/acsami.1c21850.

[4] S. Luo, Z. Zeng, G. Zeng, Z. Liu, R. Xiao, M. Chen, L. Tang, W. Tang, C. Lai, M. Cheng, B. Shao, Q. Liang, H. Wang, D. Jiang, Metal Organic Frameworks as Robust Host of Palladium Nanoparticles in Heterogeneous Catalysis: Synthesis, Application, and Prospect, ACS Appl. Mater. Interfaces. 11 (2019) 32579–32598. https://doi.org/10.1021/acsami.9b11990.

[5] T. Yang, J. Wei, Z. Sun, Y. Li, Z. Liu, Y. Xu, G. Chen, T. Wang, H. Sun, Z. Cheng, Design of oxygen vacancy in BiFeO3-based films for higher photovoltaic performance, Appl. Surf. Sci. 575 (2022) 151713. https://doi.org/10.1016/j.apsusc.2021.151713.

[6] F. Le Formal, S.R. Pendlebury, M. Cornuz, S.D. Tilley, M. Grätzel, J.R. Durrant, Back Electron–Hole Recombination in Hematite Photoanodes for Water Splitting, J. Am. Chem. Soc. 136 (2014) 2564–2574. https://doi.org/10.1021/ja412058x.

[7] L. Li, X. Sun, T. Xian, H. Gao, S. Wang, Z. Yi, X. Wu, H. Yang, Template-free synthesis of Bi 2 O 2 CO 3 hierarchical nanotubes self-assembled from ordered nanoplates for promising photocatalytic applications, Phys. Chem. Chem. Phys. 24 (2022) 8279–8295. https://doi.org/10.1039/D1CP05952A.

[8] A. Kumar, P. Choudhary, A. Kumar, P.H.C. Camargo, V. Krishnan, Recent Advances in Plasmonic Photocatalysis Based on TiO 2 and Noble Metal Nanoparticles for Energy Conversion, Environmental Remediation, and Organic Synthesis, Small. 18 (2022) 2101638. https://doi.org/10.1002/smll.202101638.

[9] R. Kumar, D. Das, A.K. Singh, C2N/WS2 van der Waals type-II heterostructure as a promising water splitting photocatalyst, J. Catal. 359 (2018) 143–150. https://doi.org/10.1016/j.jcat.2018.01.005.

[10] M.M. Obeid, A. Bafekry, S. Ur Rehman, C.V. Nguyen, A type-II GaSe/HfS2 van der Waals heterostructure as promising photocatalyst with high carrier mobility, Appl. Surf. Sci. 534 (2020) 147607. https://doi.org/10.1016/j.apsusc.2020.147607.

[11] J. Sun, Y. Hou, Z. Yu, L. Tu, Y. Yan, S. Qin, S. Chen, D. Lan, H. Zhu, S. Wang, Visible-light-driven Z-scheme Zn3In2S6/AgBr photocatalyst for boosting simultaneous Cr (VI) reduction and metronidazole oxidation: Kinetics, degradation pathways and mechanism, J. Hazard. Mater. 419 (2021) 126543. https://doi.org/10.1016/j.jhazmat.2021.126543.

551 [12] W. Yu, S. Zhang, J. Chen, P. Xia, M. H. Richter, L. Chen, W. Xu, J. Jin, S. Chen, T. Peng, Biomimetic Z-scheme
552 photocatalyst with a tandem solid-state electron flow catalyzing H 2 evolution, J. Mater. Chem. A. 6 (2018) 15668–15674.
553 https://doi.org/10.1039/C8TA02922A.

554 [13] V. Dutta, S. Sharma, P. Raizada, R. Kumar, V.K. Thakur, V.-H. Nguyen, A.M. Asiri, A.A.P. Khan, P. Singh, Recent
555 progress on bismuth-based Z-scheme semiconductor photocatalysts for energy and environmental applications, J.
556 Environ. Chem. Eng. 8 (2020) 104505. https://doi.org/10.1016/j.jece.2020.104505.

557 [14] D. Huang, S. Chen, G. Zeng, X. Gong, C. Zhou, M. Cheng, W. Xue, X. Yan, J. Li, Artificial Z-scheme
558 photocatalytic system: What have been done and where to go?, Coord. Chem. Rev. 385 (2019) 44–80.
559 https://doi.org/10.1016/j.ccr.2018.12.013.

560 [15] B. Gao, Y. Pan, Q. Chang, Z. Xi, H. Yang, Hierarchically Z-scheme photocatalyst of {010}BiVO4/Ag/CdS with
561 enhanced performance in synergistic adsorption-photodegradation of fluoroquinolones in water, Chem. Eng. J. 435 (2022)
562 134834. https://doi.org/10.1016/j.cej.2022.134834.

563 [16] C. Piao, L. Chen, Z. Liu, J. Tang, Y. Liu, Y. Lin, D. Fang, J. Wang, Construction of solar light-driven dual Z-scheme
564 Bi2MoO6/Bi2WO6\AgI\Ag photocatalyst for enhanced simultaneous degradation and conversion of nitrogenous organic
565 pollutants, Sep. Purif. Technol. 274 (2021) 119140. https://doi.org/10.1016/j.seppur.2021.119140.

566 [17] H. Chen, Y. Xing, S. Liu, Y. Liang, J. Fu, L. Wang, W. Wang, Mechanistic insights into efficient photocatalytic
567 H2O2 production of 2D/2D g-C3N4/In2S3 photocatalyst by tracking charge flow direction, Chem. Eng. J. 462 (2023)
568 142038. https://doi.org/10.1016/j.cej.2023.142038.

569 [18] C. Xing, Z. Wu, D. Jiang, M. Chen, Hydrothermal synthesis of In 2 S 3 /g-C 3 N 4 heterojunctions with enhanced
570 photocatalytic activity, J. Colloid Interface Sci. 433 (2014) 9–15. https://doi.org/10.1016/j.jcis.2014.07.015.

571 [19] Z. He, M.S. Siddique, H. Yang, Y. Xia, J. Su, B. Tang, L. Wang, L. Kang, Z. Huang, Novel Z-scheme
572 In2S3/Bi2WO6 core-shell heterojunctions with synergistic enhanced photocatalytic degradation of tetracycline
573 hydrochloride, J. Clean. Prod. 339 (2022) 130634. https://doi.org/10.1016/j.jclepro.2022.130634.

574 [20] Y. Tsujimoto, H. Hashizume, M. Yamazaki, Superoxide radical scavenging activity of phenolic compounds, Int. J.
575 Biochem. 25 (1993) 491–494. https://doi.org/10.1016/0020-711x(93)90655-x.

576 [21] K. Govindan, D.-G. Kim, S.-O. Ko, Catalytic oxidation of acetaminophen through pristine and surface-modified
577 nitrogen-doped carbon-nanotube-catalyzed peroxydisulfate activation, J. Environ. Chem. Eng. 10 (2022) 108257.
578 https://doi.org/10.1016/j.jece.2022.108257.

579 [22] Y. Nosaka, S. Komori, K. Yawata, T. Hirakawa, A. Y. Nosaka, Photocatalytic ˙OH radical formation in TiO 2
580 aqueous suspension studied by several detection methods, Phys. Chem. Chem. Phys. 5 (2003) 4731–4735.
581 https://doi.org/10.1039/B307433A.

582 [23] K. Govindan, D.-G. Kim, S.-O. Ko, Role of N-Doping and O-Groups in Unzipped N-Doped CNT Carbocatalyst for
583 Peroxomonosulfate Activation: Quantitative Structure–Activity Relationship, Catalysts. 12 (2022) 845.
584 https://doi.org/10.3390/catal12080845.

585 [24] C. Zhao, Z. Wang, X. Li, X. Yi, H. Chu, X. Chen, C.-C. Wang, Facile fabrication of BUC-21/Bi24O31Br10

composites for enhanced photocatalytic Cr(VI) reduction under white light, Chem. Eng. J. 389 (2020) 123431. https://doi.org/10.1016/j.cej.2019.123431.

[25] K. Ishibashi, A. Fujishima, T. Watanabe, K. Hashimoto, Detection of active oxidative species in TiO2 photocatalysis using the fluorescence technique, Electrochem. Commun. 2 (2000) 207–210. https://doi.org/10.1016/S1388-2481(00)00006-0.

[26] W.-K. Jo, T.S. Natarajan, Influence of TiO2 morphology on the photocatalytic efficiency of direct Z-scheme g-C3N4/TiO2 photocatalysts for isoniazid degradation, Chem. Eng. J. 281 (2015) 549–565. https://doi.org/10.1016/j.cej.2015.06.120.

[27] J. Bao, W. Quan, Y. Ning, H. Wang, Q. Wei, L. Huang, W. Zhang, Y. Ma, X. Hu, H. Tian, Efficient Visible-Light-Driven Tetracycline Degradation and Cr(VI) Reduction over a LaNi1–xFexO3 ($0 \leqslant x \leqslant 1$)/g-C3N4 Type-II Heterojunction Photocatalyst, Inorg. Chem. 62 (2023) 1086–1094. https://doi.org/10.1021/acs.inorgchem.2c02982.

[28] T. Bavani, J. Madhavan, M. Preeyanghaa, B. Neppolian, S. Murugesan, Construction of direct Z-scheme g-C3N4/BiYWO6 heterojunction photocatalyst with enhanced visible light activity towards the degradation of methylene blue, Environ. Sci. Pollut. Res. 30 (2022) 10179–10190. https://doi.org/10.1007/s11356-022-22756-9.

[29] A. Moyseowicz, Scalable one-pot synthesis of bismuth sulfide nanorods as an electrode active material for energy storage applications, J. Solid State Electrochem. 23 (2019) 1191–1199. https://doi.org/10.1007/s10008-019-04215-7.

[30] Q.-Y. Tang, X.-L. Luo, S.-Y. Yang, Y.-H. Xu, Novel Z-scheme In2S3/BiVO4 composites with improved visible-light photocatalytic performance and stability for glyphosate degradation, Sep. Purif. Technol. 248 (2020) 117039. https://doi.org/10.1016/j.seppur.2020.117039.

[31] Z. He, H. Yang, J. Sunarso, N.H. Wong, Z. Huang, Y. Xia, Y. Wang, J. Su, L. Wang, L. Kang, Novel scheme towards interfacial charge transfer between ZnIn2S4 and BiOBr for efficient photocatalytic removal of organics and chromium (VI) from water, Chemosphere. 303 (2022) 134973. https://doi.org/10.1016/j.chemosphere.2022.134973.

[32] B. Li, C. Lai, P. Xu, G. Zeng, D. Huang, L. Qin, H. Yi, M. Cheng, L. Wang, F. Huang, S. Liu, M. Zhang, Facile synthesis of bismuth oxyhalogen-based Z-scheme photocatalyst for visible-light-driven pollutant removal: Kinetics, degradation pathways and mechanism, J. Clean. Prod. 225 (2019) 898–912. https://doi.org/10.1016/j.jclepro.2019.04.012.

[33] Y. Guo, J. Wei, Y. Liu, T. Yang, Z. Xu, Surfactant-Tuned Phase Structure and Morphologies of Cu2ZnSnS4 Hierarchical Microstructures and Their Visible-Light Photocatalytic Activities, Nanoscale Res. Lett. 12 (2017) 181. https://doi.org/10.1186/s11671-017-1868-4.

[34] J. Guo, H. Zhou, S. Ting, H. Luo, J. Liang, S. Yuan, Investigation of catalytic activity and mechanism for RhB degradation by LaMnO 3 perovskites prepared via the citric acid method, New J. Chem. 43 (2019) 18146–18157. https://doi.org/10.1039/C9NJ04330F.

[35] H. Tian, M. Liu, W. Zheng, Constructing 2D graphitic carbon nitride nanosheets/layered MoS2/graphene ternary nanojunction with enhanced photocatalytic activity, Appl. Catal. B Environ. 225 (2018) 468–476.

https://doi.org/10.1016/j.apcatb.2017.12.019.

[36] J. Bao, X. Jiang, L. Huang, W. Quan, C. Zhang, Y. Wang, H. Wang, Y. Zeng, W. Zhang, Y. Ma, S. Yu, X. Hu, H. Tian, Molybdenum disulfide loading on a Z-scheme graphitic carbon nitride and lanthanum nickelate heterojunction for enhanced photocatalysis: Interfacial charge transfer and mechanistic insights, J. Colloid Interface Sci. 611 (2022) 684–694. https://doi.org/10.1016/j.jcis.2021.12.106.

[37] A. Gurses, C. Dogar, M. Yalcin, M. Acikyildiz, R. Bayrak, S. Karaca, The adsorption kinetics of the cationic dye, methylene blue, onto clay, J. Hazard. Mater. 131 (2006) 217–228. https://doi.org/10.1016/j.jhazmat.2005.09.036.

[38] Y. Chai, Y. Chen, J. Shen, M. Ni, B. Wang, D. Li, Z. Zhang, X. Wang, Distortion of the Coordination Structure and High Symmetry of the Crystal Structure in In4SnS8 Microflowers for Enhancing Visible-Light Photocatalytic CO2 Reduction, ACS Catal. 11 (2021) 11029–11039. https://doi.org/10.1021/acscatal.1c02937.

[39] Z. He, H. Yang, N.H. Wong, L. Ernawati, J. Sunarso, Z. Huang, Y. Xia, Y. Wang, J. Su, X. Fu, M. Wu, Construction of Cu7S4@CuCo2O4 Yolk–Shell Microspheres Composite and Elucidation of Its Enhanced Photocatalytic Activity, Mechanism, and Pathway for Carbamazepine Degradation, Small. 19 (2023) 2207370. https://doi.org/10.1002/smll.202207370.

[40] S. Pasternak, Y. Paz, BiYWO6: Novel synthetic routes and their effect on visible-light photocatalysis, J. Photochem. Photobiol. Chem. 318 (2016) 14–24. https://doi.org/10.1016/j.jphotochem.2015.11.024.

[41] T. Bavani, P. Sasikala, S. Arumugam, A. Malathi, P. Praserthdam, J. Madhavan, A novel S-scheme Ws2/BiYWO6 electrostatic heterostructure for enhanced photocatalytic degradation performance towards the degradation of Rhodamine B, Environ. Sci. Pollut. Res. 30 (2022) 34468–34480. https://doi.org/10.1007/s11356-022-24614-0.

[42] H. Xu, Y. Wang, X. Dong, N. Zheng, H. Ma, X. Zhang, Fabrication of In2O3/In2S3 microsphere heterostructures for efficient and stable photocatalytic nitrogen fixation, Appl. Catal. B Environ. 257 (2019) 117932. https://doi.org/10.1016/j.apcatb.2019.117932.

[43] Y. Li, T. Li, J. Tian, X. Wang, H. Cui, TiO2 Nanobelts Decorated with In2S3 Nanoparticles as Photocatalysts with Enhanced Full-Solar-Spectrum (UV–vis–NIR) Photocatalytic Activity toward the Degradation of Tetracycline, Part. Part. Syst. Charact. 34 (2017) 1700127. https://doi.org/10.1002/ppsc.201700127.

[44] Z. He, Y. Xia, J. Su, B. Tang, Fabrication of magnetically separable NiFe2O4/Bi24O31Br10 nanocomposites and excellent photocatalytic performance under visible light irradiation, Opt. Mater. 88 (2019) 195–203. https://doi.org/10.1016/j.optmat.2018.11.025.

[45] Z. He, K. Lin, N. Hing Wong, J. Sunarso, Y. Xia, X. Fu, J. Su, Z. Huang, Y. Wang, B. Tang, Elucidation of mechanisms, pathways, and toxicity of fabricated Z-scheme KNbO3/ZnIn2S4 hollow core–shell composites for enhanced ciprofloxacin photodegradation, Chem. Eng. J. 475 (2023) 146262. https://doi.org/10.1016/j.cej.2023.146262.

[46] X. Zhang, N. Zhang, C. Gan, Y. Liu, L. Chen, C. Zhang, Y. Fang, Synthesis of In2S3/UiO-66 hybrid with enhanced photocatalytic activity towards methyl orange and tetracycline hydrochloride degradation under visible-light irradiation, Mater. Sci. Semicond. Process. 91 (2019) 212–221. https://doi.org/10.1016/j.mssp.2018.11.014.

[47] Z. Wu, X. Yuan, G. Zeng, L. Jiang, H. Zhong, Y. Xie, H. Wang, X. Chen, H. Wang, Highly efficient photocatalytic

activity and mechanism of Yb3+/Tm3+ codoped In2S3 from ultraviolet to near infrared light towards chromium (VI) reduction and rhodamine B oxydative degradation, Appl. Catal. B Environ. 225 (2018) 8–21. https://doi.org/10.1016/j.apcatb.2017.11.040.